Self-healing and corrosion-sensing coatings based on pH-sensitive MOF-capped microcontainers for intelligent corrosion control

Liu, Tong; Zhang, Dawei; Zhang, Rongjun; Wang, Jinke; Ma, Lingwei; Keil, Patrick; Mol, Arjan; Li, Xiaogang

DOI
10.1016/j.cej.2022.140335

Publication date
2023

Document Version
Final published version

Published in
Chemical Engineering Journal

Citation (APA)
Liu, T., Zhang, D., Zhang, R., Wang, J., Ma, L., Keil, P., Mol, A., & Li, X. (2023). Self-healing and corrosion-sensing coatings based on pH-sensitive MOF-capped microcontainers for intelligent corrosion control. *Chemical Engineering Journal*, *454*(3), Article 140335. https://doi.org/10.1016/j.cej.2022.140335

Chemical Engineering Journal 454 (2023) 140335

Contents lists available at ScienceDirect

Chemical Engineering Journal

journal homepage: www.elsevier.com/locate/cej

Self-healing and corrosion-sensing coatings based on pH-sensitive MOF-capped microcontainers for intelligent corrosion control

Liu Tong[a,b], Dawei Zhang[a,b,c,*], Rongjun Zhang[d], Jinke Wang[a,b], Lingwei Ma[a,b,c], Patrick Keil[e], Arjan Mol[f], Xiaogang Li[a,b,c]

[a] Beijing Advanced Innovation Center for Materials Genome Engineering, Institute for Advanced Materials and Technology, University of Science and Technology Beijing, Beijing 100083, China
[b] National Materials Corrosion and Protection Data Center, University of Science and Technology Beijing, Beijing 100083, China
[c] BRI Southeast Asia Network for Corrosion and Protection (MOE), Shunde Graduate School of University of Science and Technology Beijing, Foshan 528000, China
[d] Corrosion and Protection Center, Institute for Advanced Materials and Technology, University of Science and Technology Beijing, Beijing 100083, China
[e] BASF Coatings GmbH, Münster 48165, Germany
[f] Department of Materials Science and Engineering, Delft University of Technology, Mekelweg 2, Delft 2628CD, The Netherlands

ARTICLE INFO

Keywords:
Corrosion protection
Self-healing coatings
pH-sensitive
Corrosion-sensing
Organic coating

ABSTRACT

Organic coatings are one of the most used and versatile technologies to mitigate corrosion of metals. However, organic coatings are susceptible to defects and damages that may not be easily detected. If not repaired timely, these defects may develop into major coating failures due to corrosion occurring in the damaged region, thereby limiting the lifetime of the to be protected structure. Thus, the development of smart coatings that can accurately identify corrosion location and reliably recover the damage autonomously is of particular interest. Herein, we reported a robust, corrosion-sensing and self-healing coating which incorporated pH-sensitive ZIF-8-capped $CaCO_3$ microcontainers containing the healing agent tung oil (TO) and the corrosion indicator/inhibitor 1,10-phenanthrolin-5-amine (APhen). The spontaneous leakage of incorporated TO and APhen was restrained, and the release initiated when local pH variation occurred. The corrosion protection performance of the coatings implanted with different contents of smart microcontainers were evaluated. The intact epoxy coating containing 7.5 wt% of the microcontainers exhibited the best protection performance with low water absorption (0.65 wt%), low O_2 permeability (0.21×10^{-15} cm^3 cm cm^{-2} s^{-1} Pa^{-1}), and a high storage modulus (3.0 GPa). Electrochemical impedance spectroscopy (EIS) measurements in 3.5 wt% NaCl solution demonstrated superior durability of the composite coating after self-healing. The immersion test and neutral salt spray test confirmed the coating can accurately report corrosion sites via coloration.

1. Introduction

As a worldwide problem, corrosion of steels causes tremendous economic losses, safety hazards and environmental pollution [1]. It has been proved that coatings are the technology being utilized most for protecting steel and metal substrates [2]. Many anticorrosive coatings and paints consist of epoxy-based resin technologies, because of their excellent wear resistance, adhesion strength and chemical stability [3–5]. However, their performance may be weakened severely because of the intrinsic defects formed during application or extrinsic damages from environmental weathering or mechanical impacts. If these defects or damages are not detected in time and effectively repaired, corrosion deterioration may progress quickly and lead to loss of structural and functional integrity of applications in need of protection.

Towards minimum maintenance and maximum durability and cost efficiency, the development of smart coatings that integrates autonomous self-healing and corrosion-sensing abilities is highly desirable [6–8]. Micro/nanocontainers embedded with active agents have greatly promoted the development of smart corrosion protective coatings [9–12]. The healing process of the micro/nanocontainer-embedded smart coatings can be conveniently achieved via the release of active agents such as polymerizable materials and corrosion inhibitors to the damaged region of the coating [9,13–20]. Lang et al. [21] used linseed oil as a healing agent and prepared poly(urea–formaldehyde) (PUF)

* Corresponding author at: Beijing Advanced Innovation Center for Materials Genome Engineering, Institute for Advanced Materials and Technology, University of Science and Technology Beijing, Beijing 100083, China.
E-mail address: dzhang@ustb.edu.cn (D. Zhang).

https://doi.org/10.1016/j.cej.2022.140335
Received 13 July 2022; Received in revised form 24 October 2022; Accepted 9 November 2022
Available online 15 November 2022

microcapsules using *in situ* polymerization. The linseed oil formed a solid film within the damaged area to provide a barrier for the coating. Another desirable property of smart coatings is early corrosion detection. The mechanical damage of coating induces the release of corrosion indicators from containers. By presenting color or fluorescence changes, the coating can directly reveal the active corrosion sites and provide the information for corrosion development, which may allow workers to repair or replace damaged coatings in time [22,23]. For example, Galvão et al. prepared a corrosion-sensing nanocontainer by encapsulating phenolphthalein (PhPh) in the silica nanocontainers. After salt-spray tests, the nanocontainers-doped coating changed from colorless to pink as a result of the local alkalization at the cathodic regions on the aluminium alloy 2024 substrate [24]. Shkirskiy *et al.* reported an ion-sensitive reservoir via loading soluble molybdate corrosion inhibitors in the Zn_2Al/-layered double hydroxide (LDH) and blended the LDH reservoirs in a powder paint. The main role of the LDH reservoir is the storage and release of inhibitors on demand as a result of anion-exchange between inhibitors and corrosion-relevant anions such as chloride and/or hydroxyl anions [25].

However, directly loading the active agents such as corrosion inhibitors into the containers can easily cause their premature leakage during coating preparation or in service, which not only weakens the active corrosion protection effect but may also lower the intrinsic barrier properties of the coating itself [26]. To address this issue, micro/nanocontainers incorporated in the coating endow the ability of controllably releasing the loaded active agents under external stimulus, such as light [27,28], heat [29], corrosion potential [30], redox reactions [31], ions [32,33] and pH variation. The pH-sensitive micro/nanocontainers have attracted high interest considering that local pH values may decrease or increase substantially when corrosion occurs on the steel surface [34,35]. Thus, designing micro/nanocontainers that respond to both acidic and basic pH could increase the sensitivity of the containers towards pH variation to effectively release active agents for corrosion protection. To achieve smart releasing behaviors, stimuli-responsive 'nanovalves' were assembled onto the surface of porous/hollow micro/nanocarriers by various methods, such as surface-graft precipitation [36,37], supramolecular self-assembly [38], Layer-by-Layer (LbL) assembly [39,40] and insoluble stopper capping [41].

Metal-organic frameworks (MOFs) are crystalline porous compounds, which have great potential applications in many fields (e.g., drug delivery, chemical sensing, catalysis, gas storage, etc.) because of their large specific surface areas, high porosity and tunable cavities [42,43]. The pores in MOFs can be utilized to load many types of substances to warrant different applications [44]. Some MOFs-containing coatings have been already developed for corrosion protection [45,46]. As a typical MOF, zeolitic imidazolate framework-8 (ZIF-8), with the advantage of pH-sensitive release behavior, high chemical stabilities, and simple synthetic procedure, has been employed as an appropriate carrier for active agents [47]. For example, Yang *et al.* prepared a pH-sensitive nanocontainer by loading corrosion inhibitor benzotriazole (BTA) in the tannic acid-modified ZIF-8 nanoparticles and incorporated the nanocontainers in a waterborne epoxy coating [48]. BTA and tannic acid could be released from the nanocontainers when corrosion occurred, and formed a stable ferric tannate and BTA adsorption layer on the steel substrate, thereby endowing the coating with self-healing ability. Moreover, the tertiary amine groups in the imidazole groups in ZIF-8 also can crosslink with the polymeric matrix, thus enhancing the thermal/mechanical properties and reducing the moisture uptake of the coating [49].

In this study, we report a development of a self-healing and corrosion-sensing coating which incorporates $CaCO_3$ microcontainers containing tung oil (TO) and 1,10-phenanthrolin-5-amine (APhen), using the ZIF-8 as nano-stoppers formed at the orifices of mesoporous $CaCO_3$ microcontainers (Scheme 1). TO is a polymerizable plant oil, while APhen serves not only as a corrosion inhibitor but also as a corrosion indicator due to the red coloration from its complexation with Fe^{2+} [50]. The microcontainers (ZIF-8@Ca-TO-APhen) can control the release of the entrapped TO and APhen by pH variation. Scanning electron microscopy (SEM), transmission electron microscopy (TEM), nitrogen adsorption isotherms and Fourier transform infrared spectroscopy (FTIR) were used to verify the successful synthesis of the microcontainers. The contents of the TO and the APhen in ZIF-8@Ca-TO-APhen microcontainers were calculated by thermogravimetric analysis (TGA). The ZIF-8@Ca-TO-APhen microcontainers were dispersed into epoxy resin and coated on carbon steel. The measurements of water absorption and O_2 permeability and DMA tests were conducted to investigate the barrier and mechanical performance of coatings, respectively. The self-healing performance and the corrosion-sensing ability of the coating were studied by electrochemical analysis during exposure of the damaged coated steel to aqueous chloride solution and by optical inspection and corrosion monitoring during salt spray exposure.

2. Experimental

2.1. Materials

APhen, calcium chloride ($CaCl_2$), sodium carbonate (Na_2CO_3),

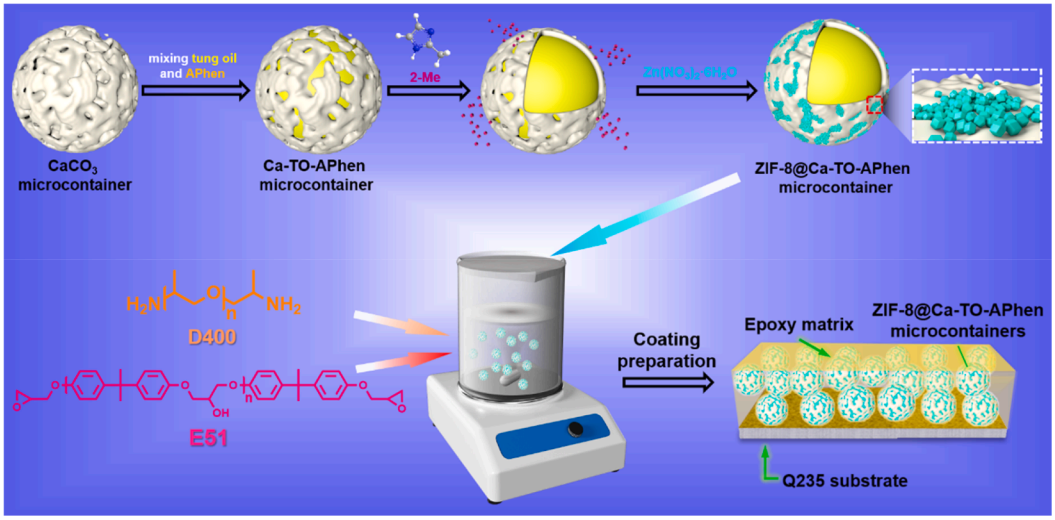

Scheme 1. Schematic illustration of the preparation process for pH-sensitive ZIF-8@Ca-TO-APhen microcontainers and ZIF-8@Ca-TO-APhen/EP coating.

sodium dodecyl sulphate (SDS), zinc nitrate hexahydrate [$Zn(NO_3)_2{\cdot}6H_2O$], 2-methylimidazole, methanol were obtained from Aladdin Industrial Corporation. Tung oil (TO) was supplied by Jinan Xinchuangyi Chemical Co. ltd. E51 epoxy resin (Bisphenol-A) and the polyetheramine curing agent (D400) were provided by Jiangsu Heli Resin Co., ltd. Deionized water was used in all experiments and all chemicals were used as received without further purification. Q235 carbon steel (99.09 % Fe, 0.45 % Mn, 0.21 % C, 0.18 % Si, 0.04 % P and 0.03 % S) was used as the substrate for the coatings.

2.2. Preparation of $CaCO_3$ microcontainers and loading of TO and APhen

According to a previously developed method [40], 3.5 g of Na_2CO_3 and 0.5 g of SDS were fully dissolved in 100 mL of deionized water. Then, $CaCl_2$ aqueous solution (100 mL, 3.7 g mL^{-1}) was injected into the aforementioned solution. After stirring for 15 min at room temperature, the $CaCO_3$ microparticles were washed by deionized water and collected by filtration and then dried at 50 ℃ overnight. The $CaCO_3$ hollow microcontainers were obtained by calcination of the $CaCO_3$ microparticles at 500 ℃ for 1 h at a heating rate of 5 ℃/min in a muffle furnace. Afterward, the $CaCO_3$ hollow microcontainers were repeatedly washed with ethanol and deionized water to remove the residuals, and then dried in a vacuum oven at 50 ℃ for 24 h.

For the loading process, 100 mg of APhen and 50 mL of TO were fully mixed in 50 mL of acetone solution, followed by the addition of 2 g of $CaCO_3$ hollow microcontainers. The mixture was placed in an airtight bottle and continuously agitated for 2 h under a vacuum with a pressure of 1.5 mbar. The loading process was repeated for 3 cycles to realize the maximum absorption of TO and APhen into $CaCO_3$ microcontainers. Afterwards, the residual TO and APhen were removed by filtration, and then the as-prepared TO/APhen-loaded $CaCO_3$ microcontainers (Ca-TO-APhen microcontainers) were dried overnight at 50 ℃.

2.3. Preparation of ZIF-8@Ca-TO-APhen microcontainers

To install ZIF-8 nano-stoppers on the surface of Ca-TO-APhen microcontainers, 100 mg of Ca-TO-APhen microcontainers were added into the 2-methylimidazole methanol solution (10 mL, 180 mg mL^{-1}) and agitated for 15 min. Then, the $Zn(NO_3)_2{\cdot}6H_2O$ methanol solution (1 mL, 100 mg mL^{-1}) was injected into the mixture. After ultrasonic treatment for 10 min, the residual chemicals were removed by centrifugation and washing. The obtained ZIF-8-capped Ca-TO-APhen microcontainers (denoted as ZIF-8@Ca-TO-APhen microcontainers) were dried overnight at 50 ℃ under vacuum. ZIF-8 capped $CaCO_3$ microcontainers (without TO and APhen) were prepared using the same procedure and were named ZIF-8@Ca microcontainers.

2.4. Preparation of epoxy composite coatings with microcontainers

First, 5 wt% ZIF-8@Ca or ZIF-8@Ca-TO-APhen microcontainers were fully mixed in the E51 epoxy resin under magnetic stirring. Then, the polyetheramine curing agent was added to the above mixture (molar ratio: E51 epoxy resin/polyetheramine curing agent = 5/3) using a mechanical agitator rotating at 500 rpm for 5 min. Before coating preparation, the steel specimens were wet-polished sequentially with 150, 240 and 400 grit sandpapers, washed with ethanol and blow-dried with nitrogen. The neat epoxy (neat EP), ZIF-8@Ca-TO-APhen$_{7.5wt\%}$/EP and ZIF-8@Ca-TO-APhen$_{10wt\%}$/EP samples were prepared by the same procedure. The obtained mixture was applied to the steel sample via a bar coater. The coating samples were obtained by drying them at room temperature for 48 h. The dry thickness of all coatings was approximately 80 μm.

2.5. Characterization of microcontainers

The structural morphology of the as-prepared microcontainers was characterized by SEM (ZEISS Gemini 300) and TEM (FEI Tecnai G2 F20). The distribution of pore size for the $CaCO_3$ hollow microcontainers was measured by mercury intrusion porosimetry (MIP, Autopore V9620) testing. The nitrogen adsorption–desorption isotherms by the Brunauer-Emmett-Teller (BET, Michael ASAP2460) method were obtained to determine the pore size distribution and pore volume of the microcontainers. The FTIR measurements of the ZIF-8@Ca-TO-APhen microcontainer, $CaCO_3$ microcontainer, ZIF-8, TO and APhen were performed with a Bruker Vertex 70 spectrometer from 4000 to 400 cm^{-1}. Thermogravimetric analysis (TGA, Netisch) was conducted to calculate the total content of TO and APhen in the microcontainers with a heating rate of 10 ℃/min from 30 to 800 ℃ under N_2 atmosphere. The release curves of APhen from Ca-TO-APhen and ZIF-8@Ca-TO-APhen microcontainers were obtained by UV–vis spectroscopy (PE, Lambda1050) in 3.5 wt% NaCl solution at different pH values.

2.6. Barrier and mechanical properties of coatings

A Sartorius BS124S microbalance was used for measuring the water absorption of the neat EP coating and the composite coatings with different amounts of ZIF-8@Ca-TO-APhen microcontainers. Different free-standing films were immersed in deionized water and weighed at different immersion time to obtain water absorption. The water absorption (Q_t) value was calculated by the equation [51]:

$$Q_t = \frac{m_t - m_0}{m_0} \tag{1}$$

where m_t and m_0 are the mass of the sample after 24 h of immersion and the initial mass of the sample, respectively. O_2 permeability was tested for all samples via the differential volume-variable pressure method under room temperature at 37 % relative humidity (ASTM D1434 standard). The dynamic mechanical analysis (DMA) tests of the samples were conducted by a DMA Q800 in tensile mode. The TO distribution in the scratch on coated steel was determined by an Agilent Cary 620 FTIR system. To observe the healing effect of the damaged coating, the cross-section of the scratched coating was obtained by the focused ion beam (FIB, Helios G4 PFIB) milling at 30 kV and 15nA upon tilting the sample at ± 50° from the substrate.

2.7. EIS measurements of coatings

To study the corrosion protection properties, EIS measurements were performed in a 3.5 wt% NaCl solution on the coatings with/without an artificial defect applied on Q235 steel during a 70 day exposure time. The EIS results were obtained using a CHI-660E electrochemical workstation with a three-electrode cell system using a coated steel substrate as a working electrode, a platinum plate electrode as a counter electrode and a saturated calomel electrode (SCE) as a reference electrode. The EIS results were tested in the $10^{-2} \sim 10^5$ Hz range with a 20 mV root mean square amplitude. The measurements were conducted on coated steels at least twice to ensure the reliability and reproducibility of the EIS data.

2.8. Corrosion-sensing and self-healing properties of coatings

To study the self-healing and corrosion-sensing properties of the composite coatings, corrosion monitoring sensors were coated with neat EP and microcontainer/EP coatings to evaluate the variation of output corrosion currents. As shown in **Fig. S1**, the corrosion monitoring sensor consists of seven pairs of Fe/graphite galvanic couples [52]. A galvanic corrosion current would be produced when an electrolyte thin liquid film was generated across the surfaces of adjacent steel and graphite electrodes. To monitor the self-healing and corrosion-sensing behaviors, an artificial scratch was made on the coating surface across seven pairs of Fe/graphite electrode couples (around 100 μm wide). The coated steels were exposed to 3.5 wt% NaCl salt spray for 80 days.

3. Results and discussion

3.1. Characterization of the microcontainers

The morphology of the $CaCO_3$ microcontainers before and after ZIF-8 installation were observed by SEM and TEM. The SEM images in Fig. 1**a** show that the $CaCO_3$ microcontainers are porous spherical microparticles with a diameter of around 5 μm. Some of the microcontainers are broken and the large cavity is exposed after mechanical impact (Fig. 1**b**, yellow circles), confirming a hollow structure of $CaCO_3$ microcontainers. Because masses of slit-shaped pores and macropores were clearly observed from the SEM images of $CaCO_3$ microcontainers, the pore information was measured by MIP. According to Fig. 1**e**, the total pore surface area and average pore diameter were 11.00 m^2/g and 343.31 nm for $CaCO_3$ microcontainers, respectively, and the porosity of $CaCO_3$ microcontainers reached 64.1 %. The MIP result demonstrated that macropores dominated the inner porous space of $CaCO_3$ microcontainers, although there were some mesopores. In Fig. 1**c**, the TEM image further reveals the nanopores on the outer surface of the $CaCO_3$ microcontainers and the hollow structure. Although the hollow structure is beneficial for the storage of drugs, the open pores on the surface of the $CaCO_3$ microcontainers readily lead to premature leakage of the core material during coating preparation or practical use. After assembly of ZIF-8 nanoparticles, it was observed that the nanopores on the surface of the microcontainer were completely sealed (Fig. 1**d**). Furthermore, the loading capacity and sealing effect of the microcontainer after installation of the ZIF-8 particles were investigated by the BET method. As seen in Fig. 1**f**, the isotherm of the ZIF-8@Ca microcontainers was a type Ⅳ isotherm with H3 type hysteresis loop, which confirms the formation of mesoporous structures in the microcontainers [40,53].

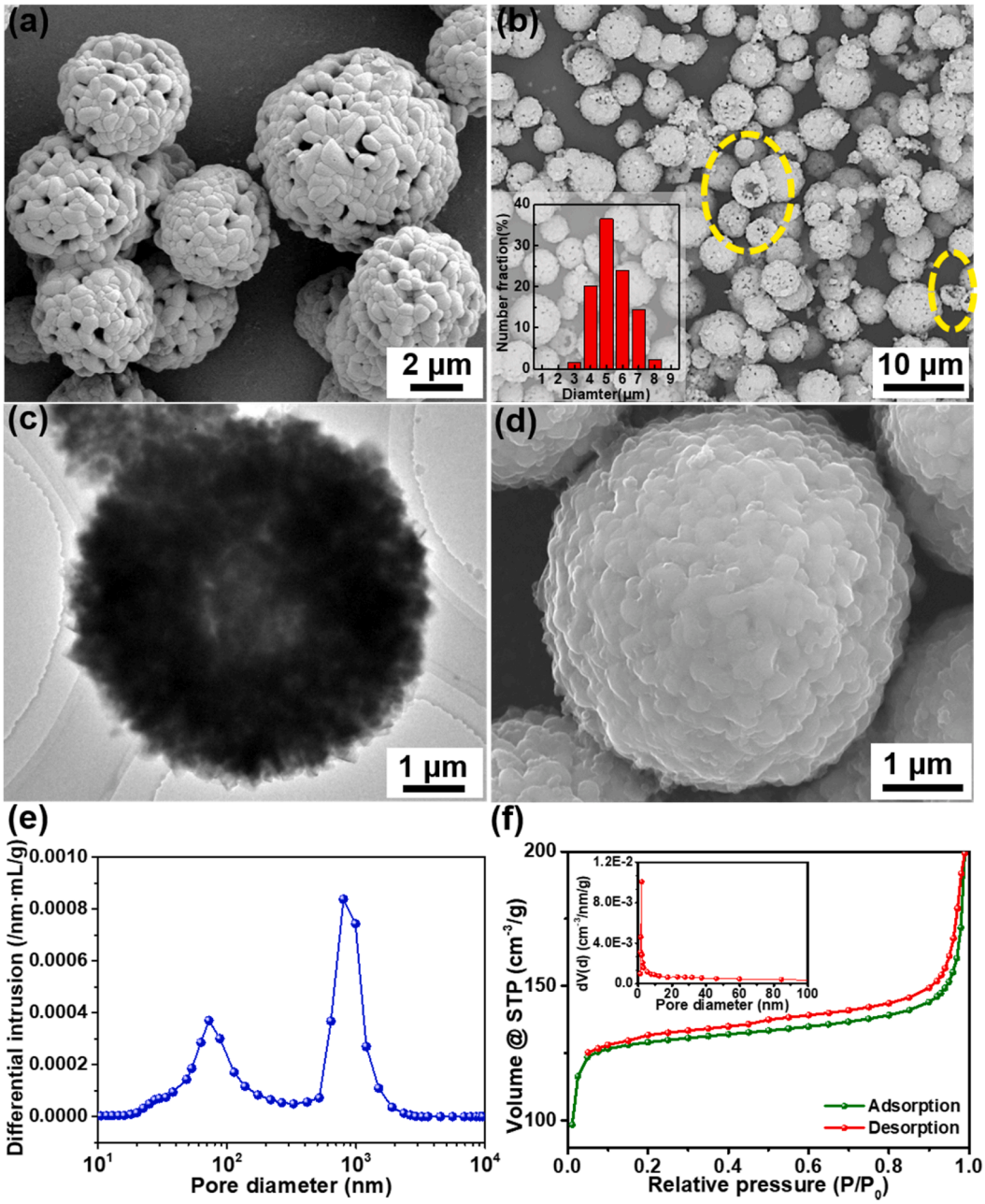

Fig. 1. (a, b) SEM images of $CaCO_3$ microcontainers, inset in the bottom-left corner in (b): size distribution of the corresponding microcontainers; (c) TEM images of the $CaCO_3$ microcontainer; (d) SEM image of ZIF-8@Ca microcontainers; (e) Pore size distribution of the $CaCO_3$ hollow microcontainers obtained by MIP; (f) N_2 adsorption–desorption isotherm and pore distribution curve of ZIF-8@Ca microcontainers.

Calculated by the N_2 absorption/desorption isothermal curves, the average pore size and pore volume of the ZIF-8@Ca microcontainers were 2.28 nm and 0.32 $cm^3\ g^{-1}$, respectively. The extremely small pore size indicates successful capping of the porous $CaCO_3$ microcontainers. Besides, a combination of large pore volume and cavity structure illustrates a good drug-loading capacity of this microcontainer.

After the loading of the core materials (TO and APhen) and the installation of ZIF-8 nanoparticles, the size of the ZIF-8@Ca-TO-APhen microcontainers (around 6 μm) was slightly larger than the $CaCO_3$ microcontainers (Fig. 2**a and 2b**). Besides, the modification by the ZIF-8 resulted in the sealing of the surface of the ZIF-8@Ca-TO-APhen microcontainers. The TEM image in Fig. 2**c** further proved that the solid and surface-sealed microparticle was obtained after the loading of the core materials and the ZIF-8 treatment. The size of densely arranged nanoparticles observed from the edge of the ZIF-8@Ca-TO-APhen microcontainer (Fig. 2**d**) was 152 nm, which was similar to that of the individual ZIF-8 nanoparticle (**Fig. S2**). In Fig. 2**d**, the EDS mapping of the edge of the microcontainer showed evenly distributed Zn element. These results further verified the successful coverage of ZIF-8 nanoparticles on the surface of the $CaCO_3$ microcontainer. In addition, the average pore size and pore volume of the ZIF-8@Ca microcontainers were 2.45 nm and 0.07 $cm^3\ g^{-1}$, respectively (Fig. 2**e**). The results showed that the pore volume value for ZIF-8@Ca-TO-APhen microcontainers was obviously lower than that for ZIF-8@Ca microcontainers (Fig. 1**f**), whereas the average pore size showed minimal changes. These results suggested that microcontainers were filled successfully.

FTIR spectra of the ZIF-8@Ca-TO-APhen microcontainer, $CaCO_3$ microcontainer, ZIF-8, TO and APhen were depicted in Fig. 3. Specifically, the strong peaks at 712, 876 and 1437 cm^{-1} are assigned to the out-of-plane bending vibration, asymmetric stretch vibration and in-plane bending vibration of the carbonate in $CaCO_3$, respectively [54]. The absorption peak observed at 420 cm^{-1} is attributed to the stretching vibration of Zn-N [55]. The appearance of the peaks at 991 and 1140 cm^{-1} are assigned to the C—N in-plane bending in the ZIF-8 structure [55]. These new peaks reflect the presence of $CaCO_3$ and ZIF-8 in the ZIF-8@Ca-TO-APhen microcontainer. As for the core materials, the TO-related characteristic peaks in the spectra of the ZIF-8@Ca-TO-APhen microcontainer include the stretching vibration peak of C═O at 1745 cm^{-1} is the asymmetric and symmetric stretching vibration peaks of saturated C—H at 2855 and 2926 cm^{-1}, respectively, and the stretching vibration peak of unsaturated C—H at 3015 cm^{-1} [56]. In addition, two new peaks are found for ZIF-8@Ca-TO-APhen microcontainers at 843 and 1637 cm^{-1}, which are related to the C—H deformation vibration and the C═N stretching vibration of the phenyl ring in APhen molecules, respectively [57]. These characteristic peaks proved that TO and APhen were successfully encapsulated in the microcontainers. Furthermore, the contents of TO and APhen in the microcontainers were calculated by TGA analysis (**Fig. S3**), which reached 13.6 wt% and 19.4 wt%, respectively.

Fig. 4**a and b** present the cumulative release of the APhen molecules from Ca-TO-APhen microcontainers and ZIF-8@Ca-TO-APhen microcontainers under pH values from 3 to 9, which is a usual pH range resulting from the corrosion reactions in coating damage [35]. For Ca-TO-APhen microcontainers (Fig. 4**a**), over 70 % of the APhen molecules loaded in the microcontainers were released after 24 h under all pH conditions, which is difficult to achieve the purpose of long-lasting corrosion protection. Notably, the cumulative release of APhen reached over 85 % after 1 day at pH = 3, which was much higher than that at pH = 7 or 9. This accelerated phenomenon may be related to the dissolution of the $CaCO_3$ structure under an acidic environment. The APhen in the Ca-TO-APhen microcontainers was fully released after 5 days of immersion under all pH conditions, which indicates the rapid leakage of the core material from the microcontainer without the protection by the ZIF-8 nano-stoppers. In contrast, the release curve of ZIF-8@Ca-TO-APhen microcontainers showed a slow rise at pH = 7 during 80 days of immersion, and the total loss of APhen was only 21.1 % (Fig. 4**b**), indicating that APhen molecules were successfully entrapped within the microcontainers with only a slight leakage. However, under acidic or alkaline conditions, the release curves of APhen in ZIF-8@Ca-TO-APhen microcontainers presented accelerated trends in varying degrees (Fig. 4**b**). Particularly, APhen was nearly completely released from ZIF-8@Ca-TO-APhen microcontainers at pH = 3 or 4 within around 36 days. Under alkaline (pH = 9) and weak acidic (pH = 5, pH = 6) conditions, the APhen molecules were released slowly, and more than half of the release can also be achieved within 80 days. At pH = 8, 49.3 % of APhen was released after 80 days. After 80 days of immersion in the solutions at pH = 3, 7 and 9, the microcontainers were collected and examined by TEM (Fig. 4**c** ~ **e**). Fig. 4**c** shows that the ZIF-8 structure and $CaCO_3$ shell were dissolved after immersion in the acidic environment. The dissolution behavior of the ZIF-8@Ca-TO-APhen

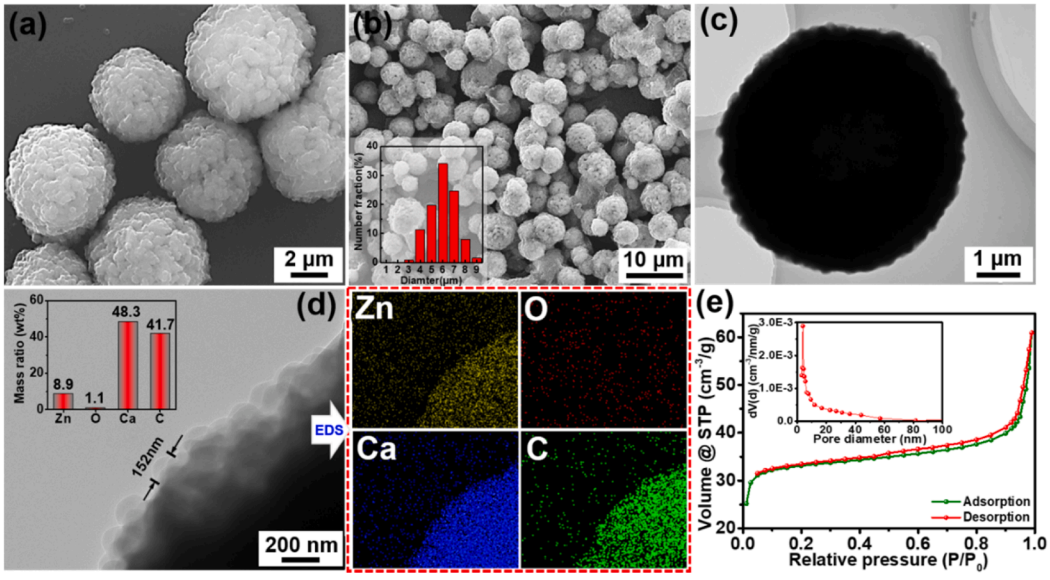

Fig. 2. SEM images of (a, b) ZIF-8@Ca-TO-APhen microcontainers, inset in the bottom-left corner in (b): size distribution of the corresponding microcontainers; TEM images of (c) ZIF-8@Ca-TO-APhen microcontainer; (d) TEM image and EDS maps of the edge of the ZIF-8@Ca-TO-APhen microcontainer. (e) N_2 adsorption–desorption isotherm and pore distribution curve of ZIF-8@Ca-TO-APhen microcontainers.

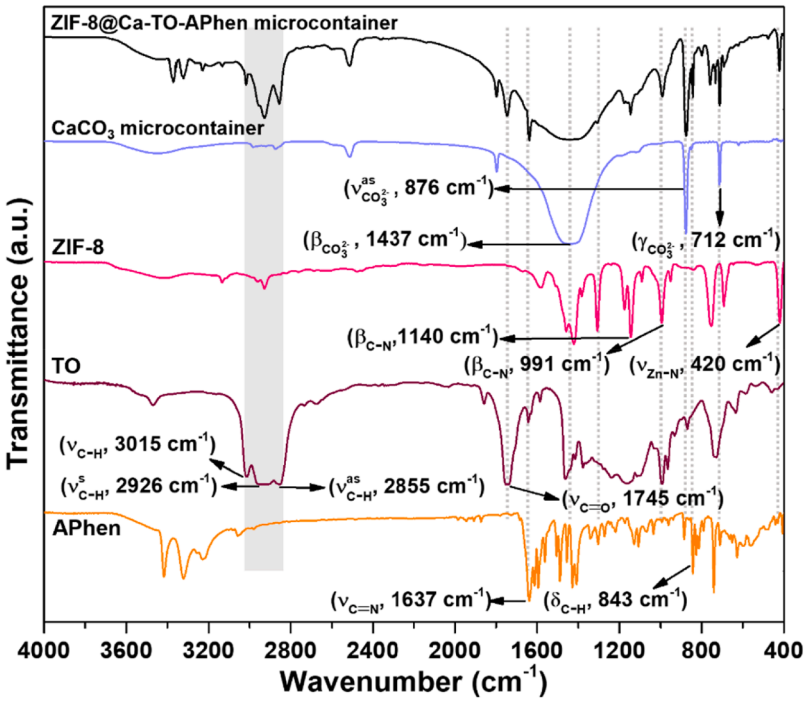

Fig. 3. FTIR spectra of ZIF-8@Ca-TO-APhen microcontainer, $CaCO_3$ microcontainer, ZIF-8, TO and APhen.

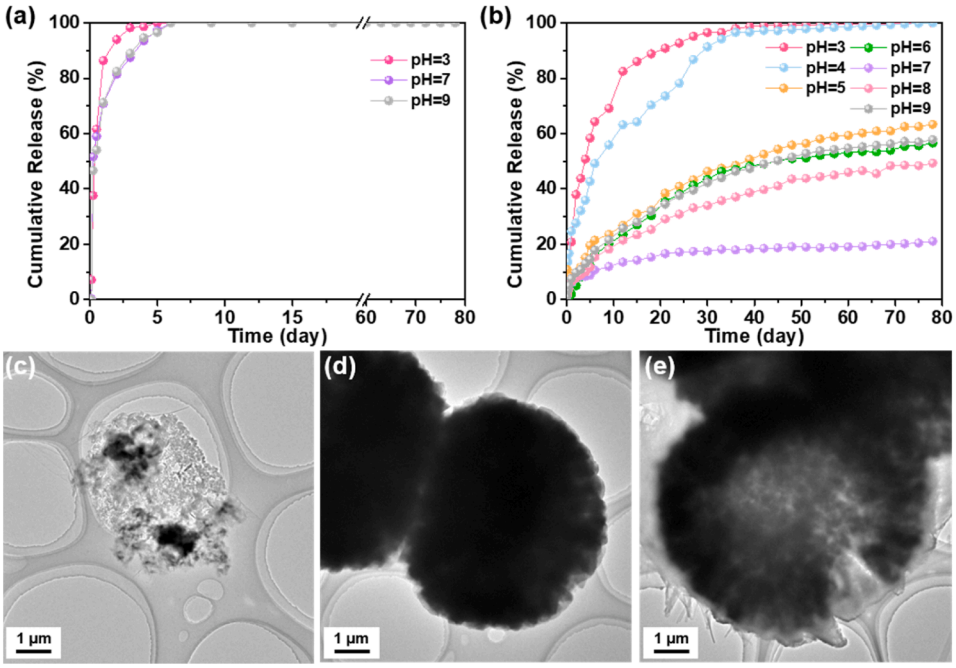

Fig. 4. The release curves of APhen molecules from (a) Ca-TO-APhen microcontainers and (b) ZIF-8@Ca-TO-APhen microcontainers at different pH conditions in 3.5 wt% NaCl solution; TEM images of ZIF-8@Ca-TO-APhen microcontainer dispersed in 3.5 wt% NaCl solution with different pH values, (c) pH = 3, (d) pH = 7 and (e) pH = 9.

microcontainers at pH = 3 was studied, as shown in **Fig. S4**. The $CaCO_3$ framework decomposed faster than ZIF-8 nanoparticles at pH = 3 (Fig. S4**b**). The ZIF-8 particles gradually dissolved with time (from 25 d to 40 d), and finally collapsed after 80 d (Fig. S4**d**). However, the alkaline condition can dissolve the ZIF-8 nano-stoppers but preserve the skeleton of the empty $CaCO_3$ microcontainers (Fig. 4**e**). These results explained why the released rate under acidic conditions was faster than that under alkaline conditions. At pH = 7, the ZIF-8@Ca-TO-APhen microcontainers remained intact after 80 days of immersion (see Fig. 2**c and 4d**), indicating the excellent pore-sealing ability of ZIF-8 nano-stoppers.

3.2. Barrier and thermal–mechanical properties of epoxy coatings containing microcontainers

The water absorption, O_2 permeability and thermal–mechanical properties of the epoxy films containing different amounts of the microcontainers were investigated. According to Fig. 5**a**, the water

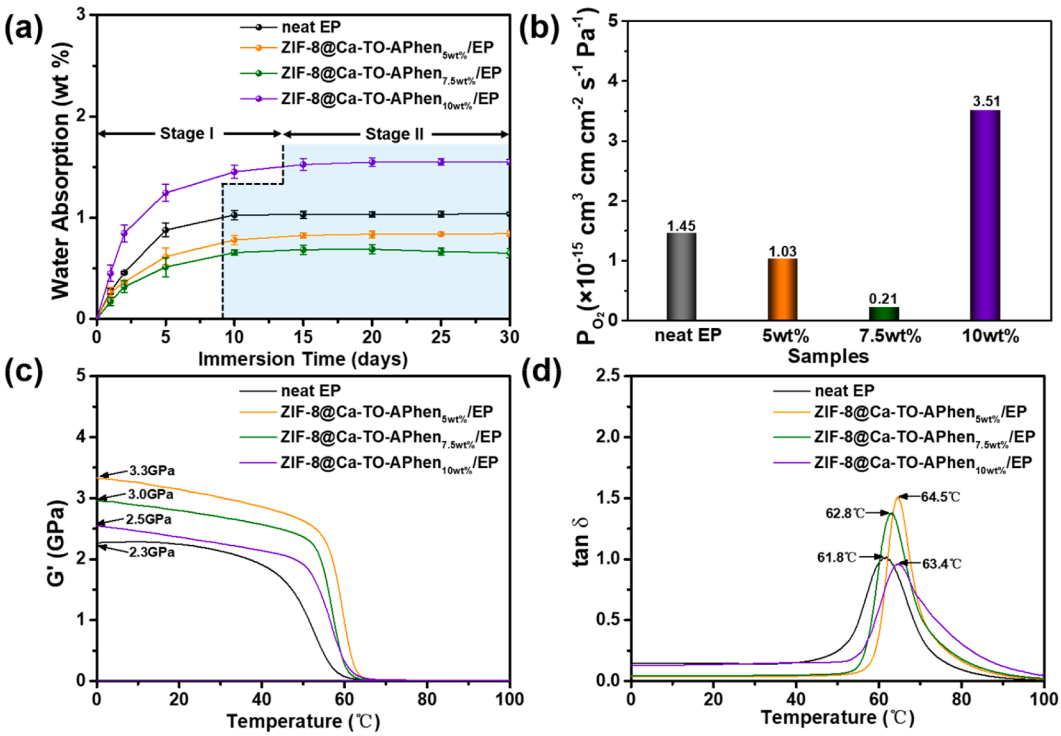

Fig. 5. (a) Water absorption and (b) O_2 permeability coefficients for different epoxy composite films. DMA curves of different samples: (c) storage modulus and (d) tan δ vs temperature.

absorption of all samples increased with a longer immersion time. After 30 days of immersion, the water absorption values for the neat epoxy (EP), ZIF-8@Ca-TO-APhen$_{5wt\%}$/EP, and ZIF-8@Ca-TO-APhen$_{10wt\%}$/EP coatings reached 1.04, 0.84, and 1.55 wt%, respectively, whereas the water absorption of the ZIF-8@Ca-TO-APhen$_{7.5wt\%}$/EP sample was only 0.65 wt%. According to Fig. 5**b**, the O_2 permeability coefficient of ZIF-8@Ca-TO-APhen$_{7.5wt\%}$/EP film was 0.21 × 10^{-15} cm^3 cm cm^{-2} s^{-1} Pa^{-1}, which was much lower than that of the other samples. The results of the water absorption and O_2 permeability tests indicated that the best barrier properties were achieved with the addition of 7.5 wt% microcontainers. The water absorption and O_2 permeability increased remarkably when 10 wt% of microcontainers were added, which may be attributed to defects in the coating network or poor dispersion of too many microcontainers in the composite film.

The effect of ZIF-8@Ca-TO-APhen microcontainers on the thermal–mechanical properties of epoxy composite films was studied by DMA (Fig. 5**c and 5d**). G' and tan δ refer to the storage modulus and the ratio of loss modulus to storage modulus, respectively. The G' and T_g values of the composite coating increased significantly with the addition of ZIF-8@Ca-TO-APhen microcontainers up to 7.5 wt%. The maximum values of G' and T_g were 3.3 GPa and 64.5℃, respectively. This result can be explained by the fact that when the content of microcapsules is in the range of 0 ~ 7.5 wt%, the uniformly dispersed microcontainers could enhance cross-linking in the epoxy network [48]. However, the G' and T_g values decreased significantly when 10 wt% microcontainers were added, which was caused by the poor dispersion of the microcontainers in the epoxy matrix.

3.3. Self-healing and corrosion-sensing performances of epoxy coatings containing microcontainers

EIS measurements were conducted on the scratched neat EP, ZIF-8@Ca$_{7.5wt\%}$/EP and ZIF-8@Ca-TO-APhen$_{7.5wt\%}$/EP coatings and the corresponding intact coatings to study the self-healing and corrosion-sensing properties. The Nyquist plots and Bode plots of the intact coatings were obtained by EIS test after 30 min of immersion in 3.5 wt% NaCl solution (Fig. 6**a** ~ **6c**). Fig. 6**d** ~ **l** show the Nyquist plots and Bode plots of the steels with scratched coatings after immersion for 1 h, 12 h, 1 d, 30 d, 50 d and 70 d, and corresponding open circuit potential (OCP) values are listed in **Table S1**. Usually, the $|Z|_{0.01Hz}$ value in the Bode plot presents a semi-quantitative estimation for corrosion resistance of a coating, i.e., a larger $|Z|_{0.01Hz}$ value reflects a higher corrosion resistance [58]. For the neat EP coating, the intact coatings initially exhibited excellent barrier performance with large capacitive arcs in the Nyquist plot (Fig. 6**a**) and the high $|Z|_{0.01Hz}$ value (4.8 × 10^9 Ω·cm^2) in the Bode plot (Fig. 6**b** ~ **c**). The phase angles in the high frequencies (10^5 Hz) are close to –90° which indicates the capacitive character of the coatings. For the scratched coating (3 mm in length, 60 μm in width, scratched area: approximately 0.18 mm^2), the size of capacitive arcs and the $|Z|_{0.01Hz}$ values were slightly increased after 1 day of immersion, which can be related to the plugging of the damaged area by the corrosion products (Fig. 6**e**). After that, the capacitive arcs of the neat EP coating shrank and the $|Z|_{0.01Hz}$ values declined gradually, indicating the continuous deterioration of the corrosion resistance (Fig. 6**d and 6e**). For the phase diagrams in Fig. 6**f**, scratched neat EP showed two-time constants including one related to the charge transfer process at the coating/substrate interface (10^{-2} ~ 10^1 Hz), and the other related to the increase of the resistance by means of corrosion product formation in the artificial defect (10^1 ~ 10^3 Hz) [59]. In contrast, the scratched ZIF-8@Ca$_{7.5wt\%}$/EP coating and neat EP coating have similar corrosion behaviors (Fig. 6**g** ~ **i**). For ZIF-8@Ca-TO-APhen$_{7.5wt\%}$/EP coating, the size of capacitive arcs was gradually enlarged during 50 days of immersion (Fig. 6**j**) and the $|Z|_{0.01Hz}$ value increased from 3.15 × 10^6 Ω·cm^2 (1st day) to 3.09 × 10^7 Ω·cm^2 after (50th day) (Fig. 6**k**), revealing a self-healing effect due to the release of TO as a healing agent and APhen as a corrosion inhibitor. The $|Z|_{0.01Hz}$ value started to decrease after immersion for a longer duration (50 ~ 70 days). As shown in Fig. 6**l**, the scratched ZIF-8@Ca-TO-APhen$_{7.5wt\%}$/EP coating exhibits a higher phase angle (–76.3°) at high frequencies (10^5 Hz) after 1 h of immersion compared with other samples, and the phase angle changed from –76.3° (1st day) to –88.0° after (50th day), indicating the capacitive properties of the coating were improving [60]. In addition, an

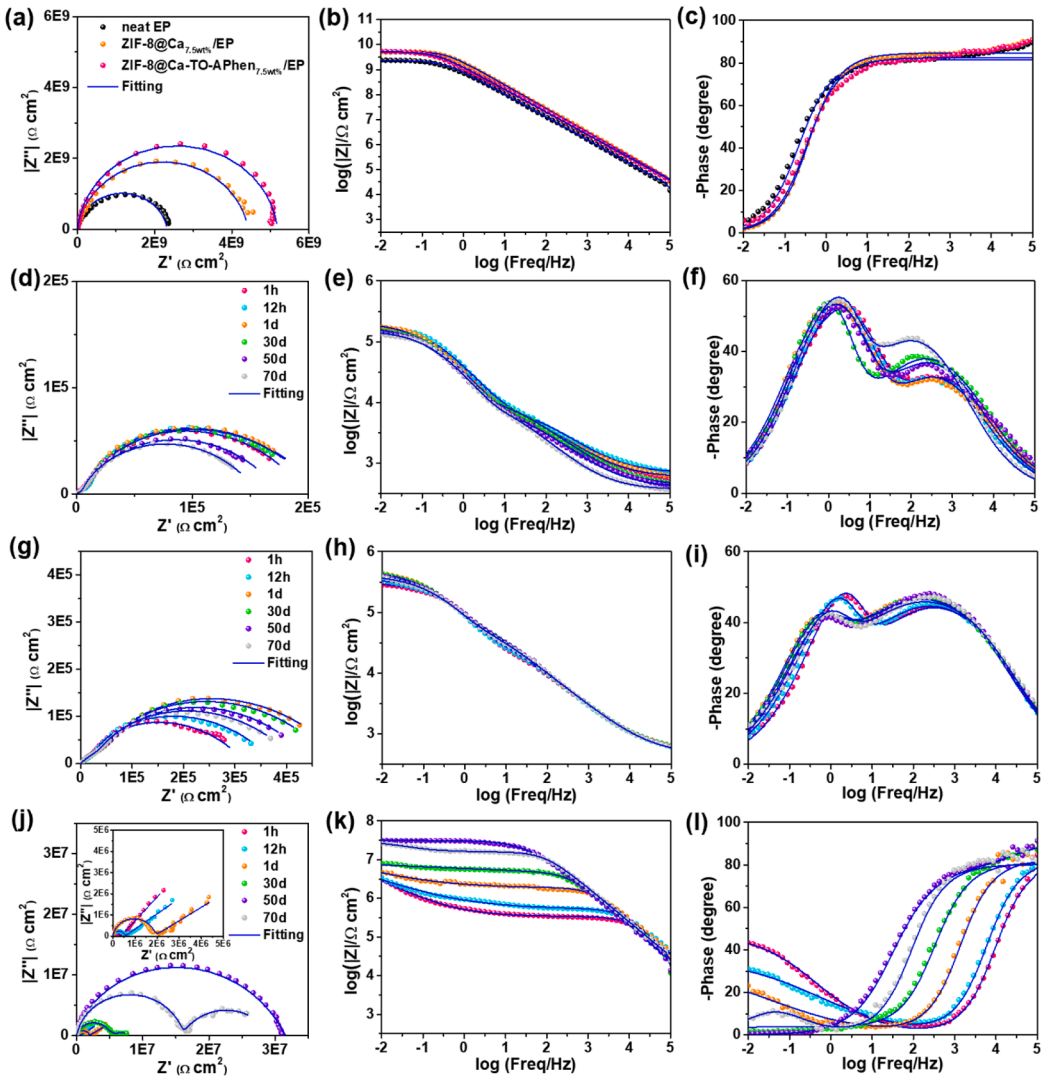

Fig. 6. Nyquist plots (a) and Bode plots (b, c) of the intact neat EP, intact ZIF-8@$Ca_{7.5wt\%}$/EP and intact ZIF-8@Ca-TO-$APhen_{7.5wt\%}$/EP coatings after 30 min of immersion in neutral 3.5 wt% NaCl solution; Nyquist plots and Bode plots of scratched neat EP (d, e and f), scratched ZIF-8@$Ca_{7.5wt\%}$/EP (g, h and i) and scratched ZIF-8@Ca-TO-$APhen_{7.5wt\%}$/EP (j, k and l) coatings during immersion in neutral 3.5 wt% NaCl solution for 70 days; Inset in the top-left corner in j: Nyquist plots of the scratched ZIF-8@Ca-TO-$APhen_{7.5wt\%}$/EP coatings after 1 h, 12 h and 1d of immersion in neutral 3.5 wt% NaCl solution.

obvious time constant at the medium–low frequencies ($10^{-2} \sim 10^{1}$) was observed at 1st h, 12th h and 1st d of immersion, which can be ascribed to steel corrosion and diffusion process of corrosion species within the coating scratch [61]. After 50 days of immersion, the peaks of the medium–low frequency time constants were observed to weaken gradually and eventually disappear. Instead, one large impendence semicircle was observed in the corresponding Nyquist plot (Fig. 6**j**) and the corresponding OCP values (Table S1) increased from –0.510 V (1st day) to –0.235 V (50th day). These results may reflect the repairing of the barrier property as TO had cured inside the coating scratch [59]. Furthermore, the phase diagrams of ZIF-8@Ca-TO-$APhen_{7.5wt\%}$/EP coating at the 70th day exhibits a distinct peak at the low-frequency region ($10^{0} \sim 10^{-2}$ Hz), revealing the corrosion activity at the interface between the metal substrate and the coating. Moreover, Fig. S5

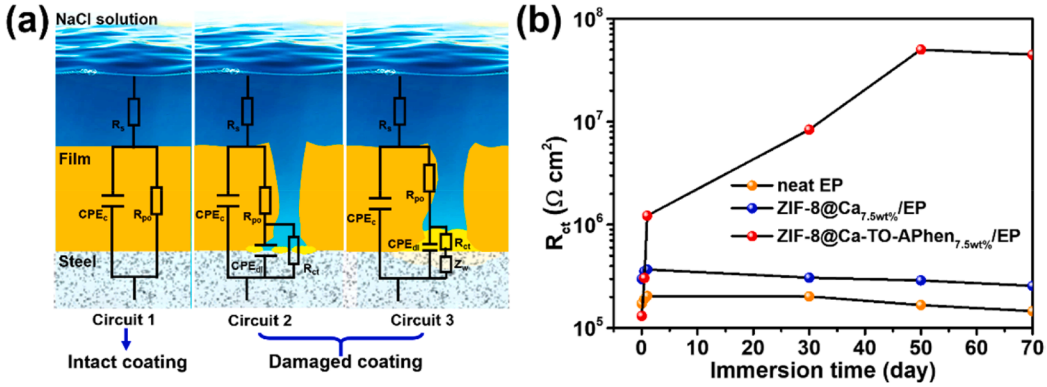

Fig. 7. (a) Equivalent electrical circuits #1–3 utilized for fitting the EIS results of intact and damaged coatings; (b) The evolution of R_{ct} values of the scratched neat EP coating, ZIF-8@$Ca_{7.5wt\%}$/EP coating and ZIF-8@Ca-TO-$APhen_{7.5wt\%}$/EP coating versus immersion time.

show Bode plots and corresponding OCP values of the different scratched coatings after 1 h, 6 h and 12 h of immersion in 3.5 wt% NaCl solution with pH = 3 or pH = 9. The Bode plots of ZIF-8 coatings under pH = 3 or pH = 9 show similar trends as in the case under neutral conditions (Fig. S5**a ~ f**) and the corresponding OCP values under pH = 3 or pH = 9 also increased to around –0.3 V (Fig. S5**g and S5h**), and confirmed that the ZIF-8@Ca-TO-APhen$_{7.5wt\%}$/EP coating can heal scratch under either acidic or basic condition.

Equivalent electrical circuits (EECs) are applied to interpret the electrochemical behavior of all coated samples (Fig. 7**a**). The solution resistance (R_s), pore resistance (R_{po}), charge transfer resistance (R_{ct}), coating capacitance (CPE_c), non-ideal double-layer capacitance (CPE_{dl}) and Warburg impedance (Z_w) parameters are involved in the circuits. For the intact coatings, the corrosion species permeate into the coating matrix through the intrinsic porosity of the epoxy matrix at the early stage of immersion. The EIS results reflecting this process could be fitted by Circuit #1 in Fig. 7**a**. Circuit #2 was used to fit the EIS results of the initial stage for scratched coated steel. In this case, the NaCl solution permeates through the coating defect and the corrosion reaction occurs on the metal surface, which is reflected by R_{ct} and CPE_{dl}. With longer immersion time, the diffusion process of corrosion species occurs at the coating scratch, which was reflected by Z_w in Circuit #3. The electrical parameters extracted based on the EECs shown in Fig. 7**a** for the all coatings are summarized in **Table S1**.

Fig. 7**b** shows the evolution of the R_{ct} value of the scratched coatings versus immersion time. Generally, a higher R_{ct} value suggests a lower corrosion rate [62]. In the early period of immersion, a slight increase can be observed for the R_{ct} values of the neat EP and the coating containing empty ZIF-8@Ca microcontainers, which may be attributed to the weak barrier effect of the accumulated rust. As the immersion time extended, the R_{ct} values of the scratched neat EP and ZIF-8@Ca/EP coatings decreased to as low as 1.46×10^5 Ω cm^2 and 2.57×10^5 Ω cm^2 after 70 days, respectively. In contrast, the R_{ct} value of the ZIF-8@Ca-TO-APhen$_{7.5wt\%}$/EP coating exhibited a substantial increase over time and reached up to 5.02×10^7 Ω cm^2 after 50 days of immersion. After 70 days of immersion, the R_{ct} value was only slightly decreased to 4.48×10^7 Ω cm^2. These results demonstrated the incorporation of ZIF-8@Ca-TO-APhen microcontainers could produce an excellent and durable self-healing effect on the corrosion resistance of the scratched coating.

Fig. 8**a ~ c** shows the morphology evolution of the coating scratches during 70 days of immersion in 3.5 wt% NaCl solution. For the neat EP coating, abundant corrosion products and large-scale corrosion spreading were observed in and around the scratch (Fig. 8**a**). In comparison, the coating containing empty ZIF-8@Ca microcontainers only exhibited relatively little rust in the scratch after 70 days of immersion, demonstrating that the corrosion on the exposed steel substrate was significantly suppressed (Fig. 8**b**). For the ZIF-8@Ca-TO-APhen$_{7.5wt\%}$/EP coating (Fig. 8**c**), after 7 days of immersion, the brownish substance was found in the scratched gap, which may be caused by the curing of tung oil in the coating scratch. No rust accumulation and corrosion spreading were observed in and around the scratch area after 50 days of immersion, confirming that the scratch on the ZIF-8@Ca-TO-APhen$_{7.5wt\%}$/EP coating was self-healed. It is also noteworthy that the scratch region showed an apparent red coloration to report corrosion after 70 days of immersion, which can be attributed to the complexation reaction of the released APhen with Fe^{2+}. The late appearance of red color agreed with the EIS results and confirmed the excellent healing effect of the corrosion resistance. Fig. 9 shows the Raman spectra of the chemical composition at the scratched region after 70 days of immersion in the 3.5 wt% NaCl solution under different conditions. For the steel without microcontainers and the steel with the addition of ZIF-8@Ca microcontainers, the main compositions are α-Fe_2O_3 (221, 276, 391, 493 and 588 cm^{-1}) and γ-FeOOH (1297 cm^{-1}) [63,64]. In comparison, the feature peaks at 1186, 1221, 1460 and 1510 cm^{-1} are observed on the steel surface in the presence of the ZIF-8@Ca-TO-APhen microcontainers and can be ascribed to the formation of the Fe^{2+}-APhen complex [65]. Besides, feature bands at 1272, 1426 and 1616 cm^{-1} are attributed to the stretching vibration of C=C, scissoring vibration of CH_2 and rocking vibration of CH=CH in the tung oil structure, respectively [66], which proved the presence of TO film.

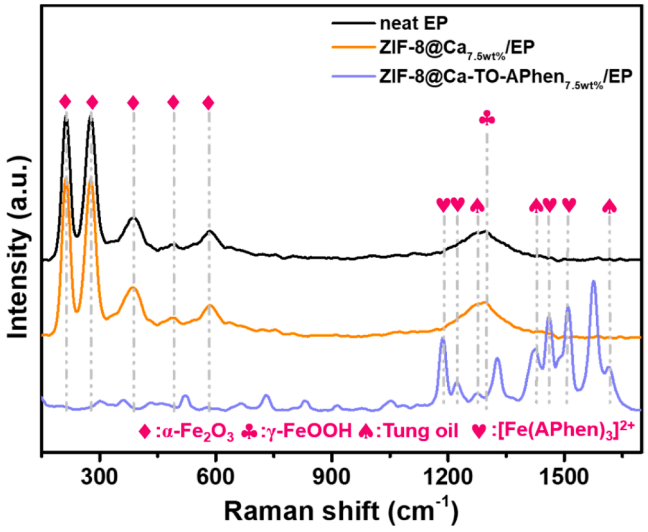

Fig. 9. Corresponding Raman spectra of the scratched center of the scratched coating after 70 days of immersion in 3.5 wt% NaCl solution.

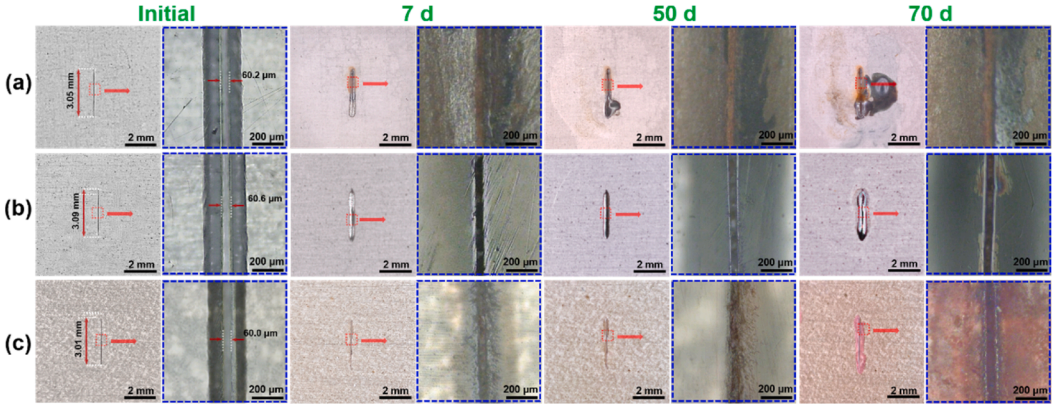

Fig. 8. Optical images of the scratched (a) neat EP coating, ZIF-8@Ca$_{7.5wt\%}$/EP coating (b), and ZIF-8@Ca-TO-APhen$_{7.5wt\%}$/EP coating (c) during 70 days of immersion in 3.5 wt% NaCl solution.

To study the healing effect of TO, Fig. 10**a** shows the mapping of the intensity of the characteristic peak of TO at 1745 cm^{-1} over the 250 μm^2 of the scratch region. The map shows a strong signal of TO along the scratch after 7 days of immersion in 3.5 wt% NaCl solution. The substance within the scratch was also tested by the FTIR spectra (Fig. 10**b (ii)**). Compared to fresh TO (Fig. 10**b (i)**), the intensities of the characteristic peaks of the filler at 1743 and 2924 cm^{-1} were weakened after 7 days of immersion, and stretching and deformation vibration peak of the vinyl groups at 991 cm^{-1} disappeared, which could be attributed to the reaction of unsaturated C=C bonds during the curing of TO at the coating scratch [56]. Besides, two characteristic peaks (1637 and 843 cm^{-1}) related to APhen were also observed in the spectra ii. These results confirmed that both TO and APhen were present in the filled scratch.

Fig. 10**c and d** present the SEM images of the top and cross-sectional views of the healed ZIF-8@Ca-TO-APhen$_{7.5wt\%}$/EP coating after 7 days of immersion in 3.5 wt% NaCl solution, respectively. The coating scratch, which had a width of around 60 μm, was fully filled. The cross section of the coatings prepared by FIB milling revealed that ZIF-8@Ca-TO-APhen microcontainers were evenly distributed throughout the coating, which could also be confirmed by the EDS mapping of Ca elements (Fig. 10**e**). The evenly distributed ZIF-8@Ca-TO-APhen microcontainers ensure that the coating damage at any region can be repaired timely.

The coated corrosion sensors were exposed to the neutral salt spray environment to monitor the coating's self-healing actions and corrosion-sensing processes. Fig. 11**a** presents the variation of the corrosion current of the sensors coated with the neat EP coating or the ZIF-8@Ca-TO-APhen$_{7.5wt\%}$/EP coating during 80 days of exposure. In the first 10 days, since the coatings were undamaged (left inset in Fig. 11**b**), the output currents from both sensors were kept at a rather low level (around 0.1nA). After 10 days, the coating surfaces were scribed to generate through-coating damages. When coating damages occurred, both sensors exhibited a sharply increased corrosion current to around 290.0nA because the steel/graphite galvanic pair was directly exposed to the salt spray environment. Subsequently, the corrosion current on the sensor with the damaged neat EP coating increased gradually from 294.3 to 533.8nA after 70 days of exposure, which was related to the continuous delamination of the damaged coating (see inset of Fig. 11**a**). In contrast, the output current of the sensor coated with the ZIF-8@Ca-TO-APhen$_{7.5wt\%}$/EP coating rapidly dropped from 300.2nA to 89.9nA was only 1.5 h, which can be attributed to the filling of TO. After 7 h of exposure, the corrosion current of the damaged coating (9.7nA) was almost the same as the intact coating. The healing effect in this period was attributed to the curing process of TO. With the increasing exposure time, unlike the neat EP coating, the ZIF-8@Ca-TO-APhen$_{7.5wt\%}$/EP coating did not exhibit any sign of corrosion (delamination or rusts) after 55 days (see inset of Fig. 11**a**).

After 60 days of salt spray exposure, the ZIF-8@Ca-TO-APhen$_{7.5wt\%}$/EP coating showed a small increase in the current (Fig. 11**c**). A distinct red color underneath the coating was observed in the scratch area after 63 days of exposure, attributing to the generation of the Fe^{2+}-APhen complex. Coating delamination can also be distinguished by the colored region underneath the intact coating area around the scratch. With the extension of the salt spray time, the colored region became larger and more pronounced. Fig. 11**d** shows the sizes of the colored areas after 63 d, 67 d and 70 d, which are linearly proportional to the magnitudes of the output current of the corrosion sensor (Fig. 11**e**). These results suggest that once the coated steel suffers from corrosion, the corrosion-sensing coating can rapidly locate corrosion and accurately reflect the degree of corrosion propagation by coloration, which is highly desirable for timely corrosion detection and maintenance in practical applications. In addition, compared with the neat EP coating, the corrosion current of the ZIF-8@Ca-TO-APhen$_{7.5wt\%}$/EP coating remained as low as 27.0nA after 70 d of salt spray exposure, which may be attributed to the corrosion inhibition effect of APhen as well [40,66].

Fig. 12 showed the dry and wet adhesion strength of the intact neat EP, ZIF-8@Ca$_{7.5wt\%}$/EP, and ZIF-8@Ca-TO-APhen$_{7.5wt\%}$/EP coating and the corresponding adhesion loss after 80 days of salt spray exposure. **Fig. S6** presents the optical images of the residual coatings after the pull-off tests. None of the samples showed cohesive failure. The dry adhesion strength of the coatings is in the following ranking: neat EP (2.98 MPa) < ZIF-8@Ca$_{7.5wt\%}$/EP (5.89 MPa) < ZIF-8@Ca-TO-APhen$_{7.5wt\%}$/EP (5.98 MPa). The epoxy coating adheres to the steel substrate via hydrogen bonding ascribed to the presence of polar functional groups. Compared with the neat EP coating, the dry adhesion strength of ZIF-

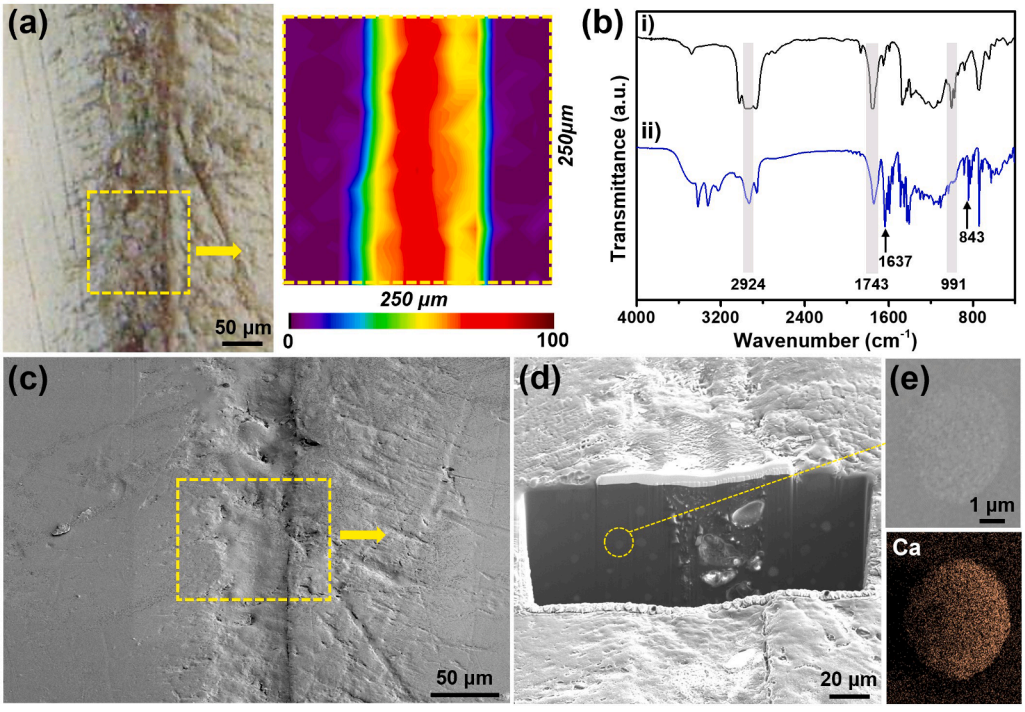

Fig. 10. (a) FTIR intensity mapping of TO at 1745 cm^{-1} in the coating scratch after 7 days of immersion in 3.5 wt% NaCl solution; (b) FTIR spectra of fresh TO (i) and filler at the scratched region (ii); (c) SEM image of the healed ZIF-8@Ca-TO-APhen$_{7.5wt\%}$/EP coating around the scratched area after 7 days of immersion in 3.5 wt% NaCl solution; (d) cross-sectional SEM image of the healed ZIF-8@Ca-TO-APhen$_{7.5wt\%}$/EP coating around the scratched area; (e) SEM image and EDS map of Ca element of a ZIF-8@Ca-TO-APhen microcontainer exposed from the cross-section of ZIF-8@Ca-TO-APhen$_{7.5wt\%}$/EP coating.

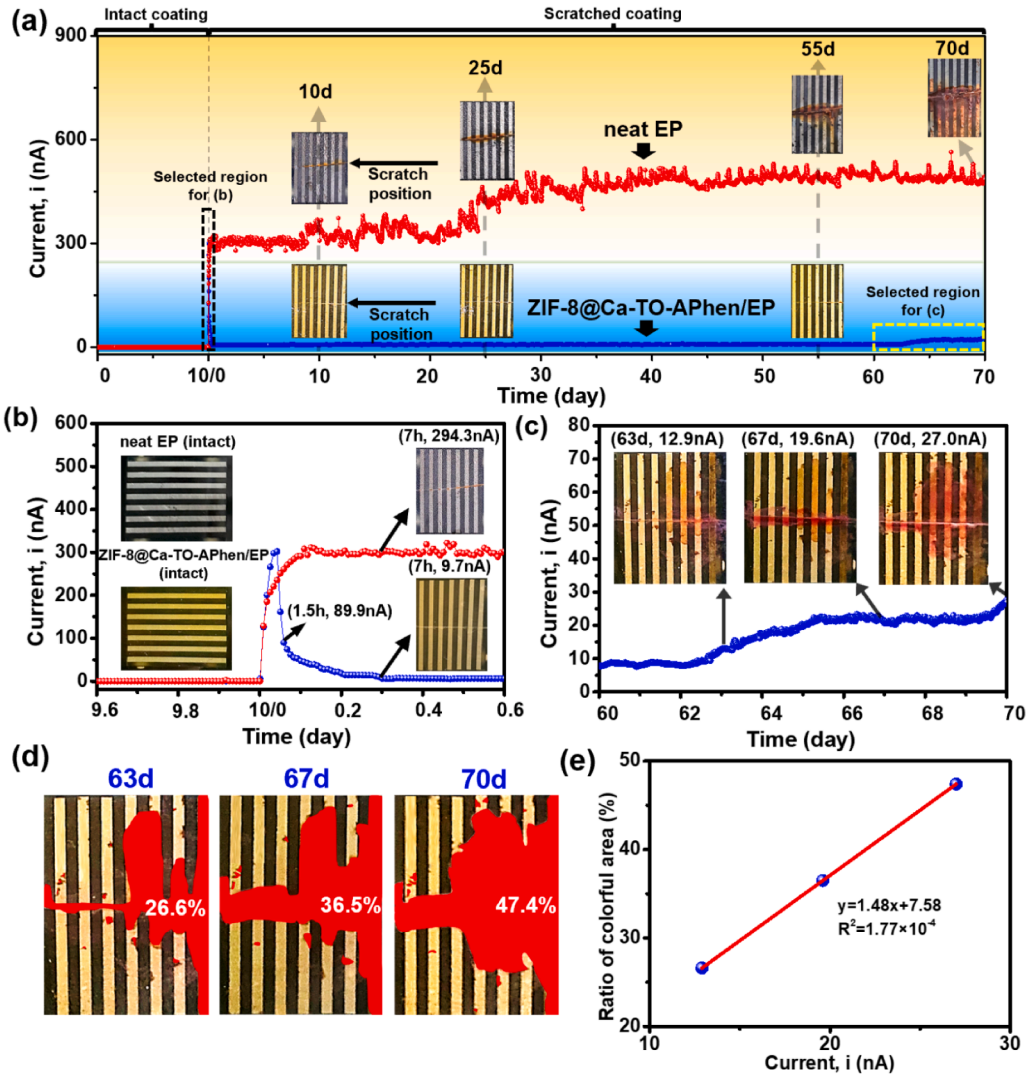

Fig. 11. (a) Optical images and the variation of corrosion currents from Fe/graphite-type galvanic corrosion sensors coated with neat EP or ZIF-8@Ca-TO-APhen$_{7.5wt\%}$/EP coating during exposure to neutral salt spray for 80 days; (b and c) Enlarged view of the selected region in Fig. 11a; (d) Propagation of the coloration underneath the coating from the scratch coating and (e) its relationship with the corrosion current.

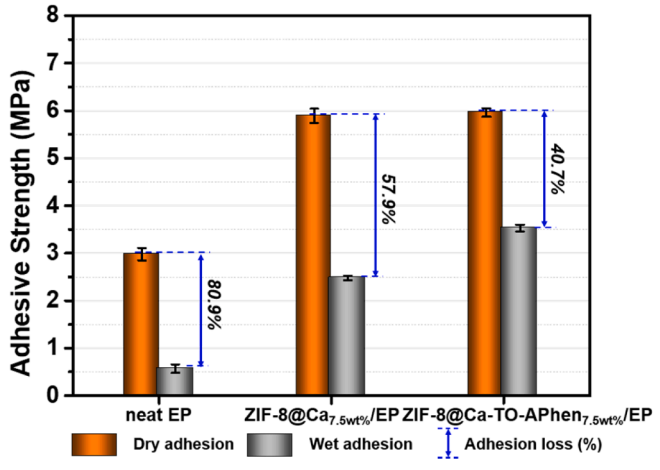

Fig. 12. The wet adhesion, dry adhesion, and adhesion loss of the (a) neat EP, (b) ZIF-8@Ca$_{7.5wt\%}$/EP, and (c) ZIF-8@Ca-TO-APhen$_{7.5wt\%}$/EP coatings before and after 80 days of salt spray exposure.

8@Ca$_{7.5wt\%}$/EP and ZIF-8@Ca-TO-APhen$_{7.5wt\%}$/EP coating was increased by around 100 %. The improvement of adhesion strength can be attributed to that the N—H groups and electron-donor sites of imidazole in the ZIF-8@Ca-TO-APhen microcontainers could react with the steel surface [67,68]. In Fig. 12, ZIF-8@Ca-TO-APhen$_{7.5wt\%}$/EP coating manifested not only the strongest wet adhesion but also the minimal adhesion loss (40.7 %) after 80 days of salt spray exposure.

3.4. *Corrosion protection, self-healing and corrosion-sensing mechanisms*

The corrosion protection, self-healing and corrosion-sensing mechanisms of the as-prepared coatings were shown in Fig. 13. In the early period, because of the high degree of crosslinking and strong adhesion strength, the intact coating exerts a significantly enhanced barrier property against corrosion species such as H_2O and O_2. The ZIF-8@Ca microcontainers served as carriers of the TO and APhen, which leached from the ruptured microspheres once the coating was damaged. Therefore, the TO healing agent and the APhen corrosion inhibitor are quickly released into the defect location. Firstly, the TO healing agent quickly covers the cracked area, and then reacts with oxygen to form a crosslinked polymer film, which can heal the crack area and protect the steel from corrosion by preventing electrolyte diffusion (Fig. 13**a**). Then,

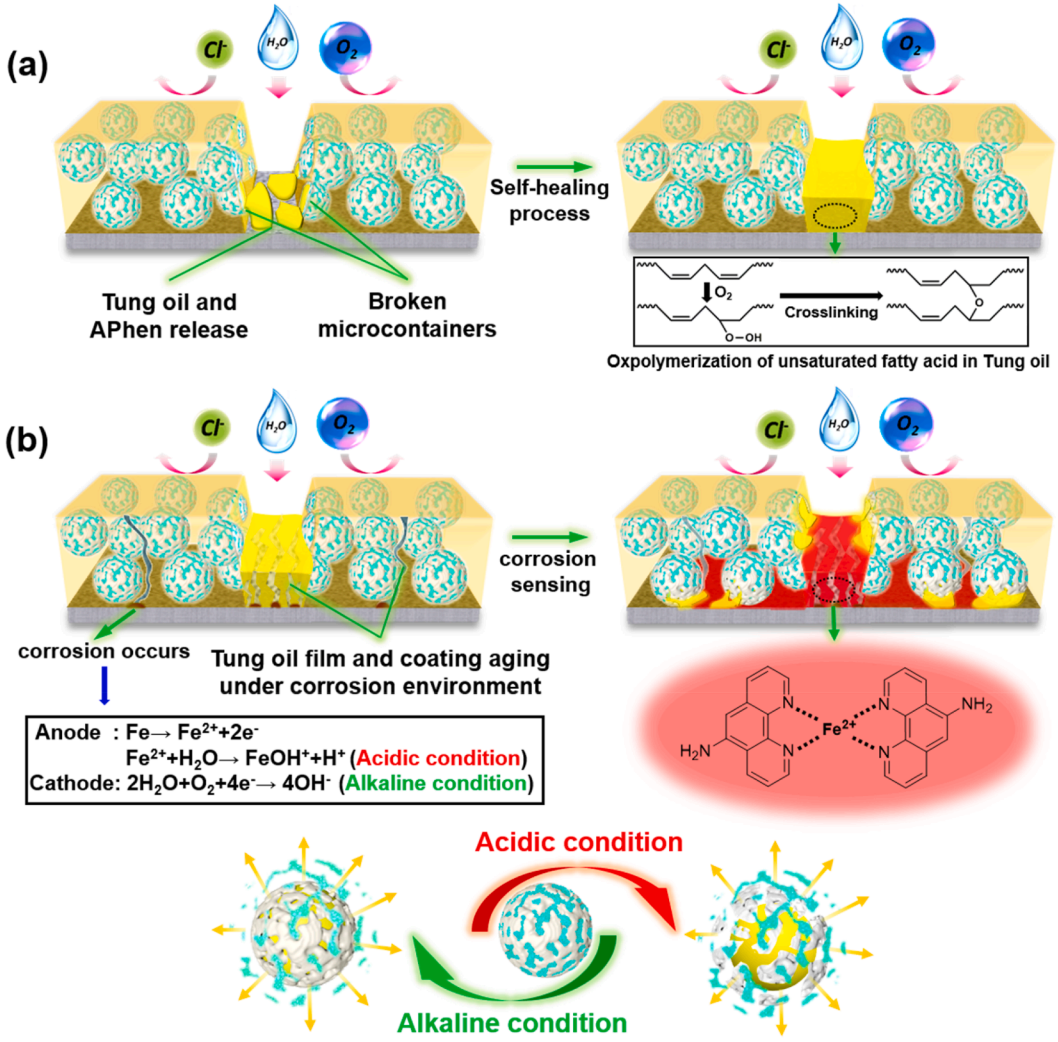

Fig. 13. Self-healing (a) and corrosion-sensing (b) mechanisms of the coating.

the APhen molecules present in the scratch region can further suppress metal corrosion under the crosslinked TO film.

As shown in Fig. 13**b**, after extended immersion, the corrosion species continuously diffuse through the healed coating, most likely via the interface between the TO film and the coating in the healed scratch [69]. When corrosion occurs at the metal-coating interfaces, the micro-anodic and micro-cathodic regions are formed at the steel surface. In anodic regions, the local pH decreases caused by the hydrolysis of the metal ions. A pH increase occurs in cathodic regions, which is attributed to the oxygen reduction reaction to produce hydroxide ions. The increased acidity/alkalinity can cause the decomposition of the capped ZIF-8 and the collapse of the ZIF-8@Ca skeleton of the ZIF-8@Ca-TO-APhen microcontainers in the coatings, triggering the release of core substances. The released APhen can be complexed with Fe^{2+} ions to form a red complex on the steel surface, which can not only inhibit corrosion but also report corrosion propagation via coloration.

4. Conclusion

In this work, we developed of a smart protective coating that integrated self-healing and corrosion-sensing capabilities based on a novel pH-sensitive ZIF-8 capped $CaCO_3$ microcontainer containing healing agent TO and APhen molecules as both inhibitor and indicator of corrosion. The as-prepared microcontainer had a good loading capacity (TO: 13.6 wt%, APhen: 19.4 wt%) and could release TO and APhen in a controlled fashion responding to pH variation. The coating with 7.5 wt% microcontainers exhibited low water absorption (0.65 wt%), low O_2 permeability (0.21×10^{-15} cm^3 cm cm^{-2} s^{-1} Pa^{-1}), and a high storage modulus (3.0 GPa). The EIS and SEM results demonstrated that the released TO from the ZIF-8@Ca-TO-APhen microcontainers could effectively fill the coating scratch and heal the corrosion resistance of the damaged coating. The $|Z|_{0.01Hz}$ value of the healed ZIF-8@Ca-TO-$APhen_{7.5wt\%}$/EP coating was increased to 3.09×10^7 Ω·cm^2 after 70 days of immersion in 3.5 wt% NaCl solution, which was more than two orders of magnitudes than that of the scratched neat EP coating. Besides, triggered by the local pH variation, the released APhen from the containers can react with Fe^{2+} ions to generate a red complex that could inhibit corrosion and accurately report corrosion propagation. The coating of this study showed high barrier performance, strong adhesion, and self-healing and corrosion-sensing properties, which offered a promising new solution for intelligent corrosion control.

Declaration of Competing Interest

The authors declare that they have no known competing financial interests or personal relationships that could have appeared to influence the work reported in this paper.

Data availability

Data will be made available on request.

Acknowledgments

This work was supported by Joint Fund of Basic and Applied Basic Research Fund of Guangdong Province (2021B1515130009) and Fundamental Research Funds for the Central Universities (FRF-BD-20-28A2).

Appendix A. Supplementary data

Supplementary data to this article can be found online at https://doi.org/10.1016/j.cej.2022.140335.

References

[1] B. Hou, X. Li, X. Ma, C. Du, D. Zhang, M. Zheng, W. Xu, D. Lu, F. Ma, The cost of corrosion in China, npj Mater Degrad. 1 (2017) 1–10.
[2] F. Zhang, P. Ju, M. Pan, D. Zhang, Y. Huang, G. Li, X. Li, Self-healing mechanisms in smart protective coatings: A review, Corros. Sci. 144 (2018) 74–88.
[3] J. Cui, Z. Xiong, H. Qiu, L. Jing, J. Yang, Functionalized graphene oxide: Carrier for corrosion inhibitor and barrier in waterborne epoxy coatings, Compos. Part A-Appl. S. 144 (2021), 106354.
[4] T. Liu, H. Zhao, D. Zhang, Y. Lou, L. Huang, L. Ma, X. Hao, L. Dong, F. Rosei, W. M. Lau, Ultrafast and high-efficient self-healing epoxy coatings with active multiple hydrogen bonds for corrosion protection, Corros. Sci. 187 (2021), 109485.
[5] X. Wang, Y. Li, C. Li, X. Zhang, D. Lin, F. Xu, Y. Zhu, H. Wang, J. Gong, T. Wang, Highly orientated graphene/epoxy coating with exceptional anti-corrosion performance for harsh oxygen environments, Corros. Sci. 176 (2020), 109049.
[6] L. Ma, C. Ren, J. Wang, T. Liu, H. Yang, Y. Wang, Y. Huang, D. Zhang, Self-Reporting Coatings for Autonomous Detection of Coating Damage and Metal Corrosion: A Review, Chem. Eng. J. 421 (2021) 127854.
[7] M. Kosarli, D. Bekas, K. Tsirka, A.S. Paipetis, Capsule-based self-healing polymers and composites, Elsevier, Self-Healing Polymer-Based Systems, 2020, pp. 259–278.
[8] J. Wang, L. Ma, X. Guo, S. Wu, T. Liu, J. Yang, C. Ren, S. Li, D. Zhang, Two birds with one stone: Nanocontainers with synergetic inhibition and corrosion sensing abilities towards intelligent self-healing and self-reporting coating, Chem. Eng. J. 433 (2022), 134515.
[9] M. Sánchez, P. Faria, L. Ferrara, E. Horszczaruk, H.M. Jonkers, A. Kwiecień, J. Mosa, A. Peled, A.S. Pereira, D. Snoeck, M. Stefanidou, T. Stryszewska, B. Zając, External treatments for the preventive repair of existing constructions: A review, Constr. Build. Mater. 193 (2018) 435–452.
[10] T. Liu, L. Ma, X. Wang, J. Wang, H. Qian, D. Zhang, X. Li, Self-healing corrosion protective coatings based on micro/nanocarriers: A review, Corros. Commun. 1 (2021) 18–25.
[11] I.I. Udoh, H. Shi, E.F. Daniel, J. Li, S. Gu, F. Liu, E.-H. Han, Active anticorrosion and self-healing coatings: a review with focus on multi-action smart coating strategies, J. Mater. Sci. Technol. 116 (2022) 224–237.
[12] A.A. Olajire, Recent advances on organic coating system technologies for corrosion protection of offshore metallic structures, J. Mol. Liq. 269 (2018) 572–606.
[13] L. Ma, J. Wang, D. Zhang, Y. Huang, L. Huang, P. Wang, H. Qian, X. Li, H.A. Terryn, J.M. Mol, Dual-action self-healing protective coatings with photothermal responsive corrosion inhibitor nanocontainers, Chem. Eng. J. 404 (2021), 127118.
[14] S.A. Haddadi, A. Ramazani, M. Mahdavian, P. Taheri, J. Mol, Y. Gonzalez-Garcia, Self-healing epoxy nanocomposite coatings based on dual-encapsulation of nano-carbon hollow spheres with film-forming resin and curing agent, Compos. B. Eng. 175 (2019), 107087.
[15] S. García, H.R. Fischer, P.A. White, J. Mardel, Y. González-García, J. Mol, A. E. Hughes, Self-healing anticorrosive organic coating based on an encapsulated water reactive silyl ester: Synthesis and proof of concept, Prog. Org. Coat. 70 (2–3) (2011) 142–149.
[16] S.A. Haddadi, A. Ramazani S. A., M. Mahdavian, P. Taheri, J.M.C. Mol, Mechanical and corrosion protection properties of a smart composite epoxy coating with dual-encapsulated epoxy/polyamine in carbon nanospheres, Ind. Eng. Chem. Res. 58 (8) (2019) 3033–3046.
[17] A. Mikhailau, H. Maltanava, S.K. Poznyak, A.N. Salak, M.L. Zheludkevich, K. A. Yasakau, M.G.S. Ferreira, One-step synthesis and growth mechanism of nitrate intercalated ZnAl LDH conversion coatings on zinc, Chem. Commun. 55 (48) (2019) 6878–6881.
[18] N. Wint, D. Eaves, G. Williams, H.N. McMurray, The use of anion exchange pigments to inhibit the filiform corrosion of zinc-aluminium-magnesium coated steel, Corros. Sci. 193 (2021), 109886.
[19] G. Williams, H.N. Mcmurray, Anion-exchange inhibition of filiform corrosion on organic coated AA2024-T3 aluminum alloy by hydrotalcite-like pigments, Electrochem. Solid-State Lett. 6 (3) (2003) B9.
[20] D. Snihirova, L. Liphardt, G. Grundmeier, F. Montemor, Electrochemical study of the corrosion inhibition ability of "smart" coatings applied on AA2024, J. Solid State Electrochem. 17 (8) (2013) 2183–2192.
[21] S. Lang, Q. Zhou, Synthesis and characterization of poly(urea-formaldehyde) microcapsules containing linseed oil for self-healing coating development, Prog. Org. Coat. 105 (2017) 99–984.
[22] D. Mata, N. Scharnagl, S. Lamaka, E. Malheiro, F. Maia, M. Zheludkevich, Validating the early corrosion sensing functionality in poly (ether imide) coatings for enhanced protection of magnesium alloy AZ31, Corros. Sci. 140 (2018) 307–320.
[23] D.A. Braasch, M. Gillis, M. Pramanik, R.C. Ferguson, D. Delatte, M. Blanton, J. W. Rawlins, Detection of in situ early corrosion on polymer-coated metal substrates, ACS Appl. Mater. Inter. 11 (40) (2019) 37193–37208.
[24] T.L.P. Galvão, I. Sousa, M. Wilhelm, J. Carneiro, J. Opršal, H. Kukačková, V. Špaček, F. Maia, J.R.B. Gomes, J. Tedim, M.G.S. Ferreira, Improving the functionality and performance of AA2024 corrosion sensing coatings with nanocontainers, Chem. Eng. J. 341 (2018) 526–538.
[25] V. Shkirskiy, P. Keil, H. Hintze-Bruening, F. Leroux, P. Vialat, G. Lefèvre, K. Ogle, P. Volovitch, Factors affecting MoO_4^{2-} inhibitor release from Zn_2Al based layered double hydroxide and their implication in protecting hot dip galvanized steel by means of organic coatings, ACS Appl. Mater. Inter. 7 (45) (2015) 25180–25192.
[26] ChenDi Ding, JianHua Xu, L. Tong, GuangCai Gong, W. Jiang, J. Fu, Design and fabrication of a novel stimulus-feedback anticorrosion coating featured by rapid self-healing functionality for the protection of magnesium alloy, ACS Appl. Mater. Inter. 9 (24) (2017) 21034–21047.
[27] M. Odarczenko, D. Thakare, W. Li, S.P. Venkateswaran, N.R. Sottos, S.R. White, Sunlight-Activated Self-Healing Polymer Coatings, Adv. Eng. Mater. 22 (3) (2020) 1901223.
[28] J. Wang, L. Ma, Y. Huang, C. Ren, H. Yang, Y. Wang, T. Liu, D. Zhang, Photothermally activated self-healing protective coating based on the "close and seal" dual-action mechanisms, Compos. Part B-Eng. 231 (2022), 109574.
[29] Y. Huang, L. Deng, P. Ju, L. Huang, H. Qian, D. Zhang, X. Li, H.A. Terryn, J.M. C. Mol, Triple-action self-healing protective coatings based on shape memory polymer (SMP) containing dual-function microspheres, ACS Appl. Mater. Inter. 10 (27) (2018) 23369–23379.
[30] T. Wang, J. Du, S. Ye, L.H. Tan, J.J. Fu, Triple stimuli-responsive smart nanocontainers enhanced self-healing anticorrosion coatings for protection of aluminum alloy, ACS Appl. Mater. Inter. 11 (4) (2019) 4425–4438.
[31] A. Vimalanandan, L.P. Lv, T.H. Tran, K. Landfester, D. Crespy, M. Rohwerder, Redox-responsive self-healing for corrosion protection, Adv. Mater. 25 (48) (2013) 6980–6984.
[32] Z. Zheng, X. Huang, M. Schenderlein, D. Borisova, R. Cao, H. Möhwald, D. Shchukin, Self-Healing and antifouling multifunctional coatings based on pH and sulfide ion sensitive nanocontainers, Adv. Funct. Mater. 23 (26) (2013) 3307–3314.
[33] Y. Huang, T. Liu, L. Ma, J. Wang, D. Zhang, X. Li, Saline-responsive triple-action self-healing coating for intelligent corrosion control, Mater. Design 214 (2022), 110381.
[34] E.V. Skorb, D. Fix, D.V. Andreeva, H. Möhwald, D.G. Shchukin, Surface-modified mesoporous SiO2 containers for corrosion protection, Adv. Funct. Mater. 19 (15) (2009) 2373–2379.
[35] M. Theerasilp, D. Crespy, Halochromic Polymer nanosensors for simple visual detection of local pH in coatings, Nano Lett. 21 (8) (2021) 3604–3610.
[36] G.L. Li, Z. Zheng, H. Mhwald, D.G. Shchukin, Silica/polymer double-walled hybrid nanotubes: synthesis and application as stimuli-responsive nanocontainers in self-healing coatings, ACS Nano 7 (3) (2013) 2470–2478.
[37] J.L. Vivero-Escoto, I.I. Slowing, C.W. Wu, S.Y. Lin, Photoinduced intracellular controlled release drug delivery in human cells by gold-capped mesoporous silica nanosphere, J. Am. Chem. Soc. 131 (10) (2009) 3462–3463.
[38] C.D. Ding, Y. Liu, M.D. Wang, T. Wang, J.J. Fu, Self-healing, superhydrophobic coating based on mechanized silica nanoparticles for reliable protection of magnesium alloys, J. Mater. Chem. A 4 (21) (2016) 8041–8052.
[39] E.M. Shchukina, D.G. Shchukin, LbL coated microcapsules for delivering lipid-based drugs, Adv. Drug Deliver. Rev. 63 (9) (2011) 837–846.
[40] T. Liu, D. Zhang, L. Ma, Y. Huang, X. Hao, H. Terryn, A. Mol, X. Li, Smart protective coatings with self-sensing and active corrosion protection dual functionality from pH-sensitive calcium carbonate microcontainers, Corros. Sci. 200 (2022), 110254.
[41] E. Abdullayev, Y. Lvov, Clay nanotubes for corrosion inhibitor encapsulation: release control with end stoppers, J. Mater. Chem. 20 (32) (2010) 6681–6687.
[42] L. Zheng, C.Z. Hua, Armored MOFs: Enforcing soft microporous MOF nanocrystals with hard mesoporous silica, J. Am. Chem. Soc. 136 (15) (2014) 5631–5639.
[43] Z. Song, Wu, Yang, Cao, Qi, Wang, Huajuan, Xiangru, Han, pH-responsive, light-triggered on-demand antibiotic release from functional metal-organic framework for bacterial infection tombination therapy, Adv. Funct. Mater. 28 (23) (2018) 1800011.
[44] S. Wang, C.M. McGuirk, A. d'Aquino, J.A. Mason, C.A. Mirkin, Metal–organic framework nanoparticles, Adv. Mater. 30 (37) (2018) 1800202.
[45] H. Chen, F. Wang, H. Fan, R. Hong, W. Li, Construction of MOF-based superhydrophobic composite coating with excellent abrasion resistance and durability for self-cleaning, corrosion resistance, anti-icing, and loading-increasing research, Chem. Eng. J. 408 (2021), 127343.
[46] H. Cai, P. Wang, D. Zhang, Y. Wang, E. Li, An intelligent self-defensive coating based on sulfide ion responsive nanocontainers for suppression of microbiologically influenced corrosion induced by sulfate reducing bacteria, Corros. Sci. 188 (2021), 109543.
[47] H. Zheng, Y. Zhang, L. Liu, W. Wan, P. Guo, A.M. Nyström, X. Zou, One-pot synthesis of metal–organic frameworks with encapsulated target molecules and their applications for controlled drug delivery, J. Am. Chem. Soc. 138(3) (2016) 962–968.

[48] C. Yang, W. Xu, X. Meng, X. Shi, L. Shao, X. Zeng, Z. Yang, S. Li, Y. Liu, X. Xia, A pH-responsive hydrophilic controlled release system based on ZIF-8 for self-healing anticorrosion application, Chem. Eng. J. 415 (2021), 128985.
[49] C. Liu, M. Mullins, S. Hawkins, M. Kotaki, H.-J. Sue, Epoxy nanocomposites containing zeolitic imidazolate framework-8, ACS Appl. Mater. Interfaces 10 (1) (2018) 1250–1257.
[50] C. Liu, H. Wu, Y. Qiang, H. Zhao, L. Wang, Design of smart protective coatings with autonomous self-healing and early corrosion reporting properties, Corros. Sci. 184 (2021), 109355.
[51] T. Liu, J. Wei, L. Ma, S. Liu, D. Zhang, H. Zhao, Effect of polyaniline-based plate on the anticorrosion performance of epoxy coating, Prog. Org. Coat. 151 (2021), 106109.
[52] Z. Pei, D. Zhang, Y. Zhi, T. Yang, L. Jin, D. Fu, X. Cheng, H.A. Terryn, J.M.C. Mol, X. Li, Towards understanding and prediction of atmospheric corrosion of an Fe/Cu corrosion sensor via machine learning, Corros. Sci. 170 (2020), 108697.
[53] Y. Shang, Y. Cui, R. Shi, P. Yang, J. Wang, Y. Wang, Regenerated WO2. 72 nanowires with superb fast and selective adsorption for cationic dye: Kinetics, isotherm, thermodynamics, mechanism, J. Hazard. Mater. 379 (2019) 120834.
[54] H.A. Al-Hosney, V.H. Grassian, Water, sulfur dioxide and nitric acid adsorption on calcium carbonate: A transmission and ATR-FTIR study, Phys. Chem. Chem. Phys. 7 (6) (2005) 1266–1276.
[55] S. Duan, B. Dou, X. Lin, S. Zhao, W. Emori, J. Pan, H. Hu, H. Xiao, Influence of active nanofiller ZIF-8 metal-organic framework (MOF) by microemulsion method on anticorrosion of epoxy coatings, Colloid. Surface. A 624 (2021), 126836.
[56] Y. Feng, Y. Cui, M. Zhang, M. Li, H. Li, Preparation of tung oil-loaded PU/PANI microcapsules and synergetic anti-corrosion properties of self-healing epoxy coatings, Macromol. Mater. Eng. 306 (2) (2021) 2000581.
[57] C. Zheng, H. Ren, Z. Cui, F. Chen, G. Hong, Synthesis and characterization of nano-scale Terbium (III)-trimesic acid (TMA)-1,10-phenanthroline(phen) luminescent complex, J. Alloy. Compd. 477 (2009) 333–336.
[58] N.P. Tavandashti, M. Ghorbani, A. Shojaei, J.M.C. Mol, H. Terryn, K. Baert, Y. Gonzalez-Garcia, Inhibitor-loaded conducting polymer capsules for active corrosion protection of coating defects, Corros. Sci. 112 (2016) 138–149.
[59] C. Oliveira, M. Ferreira, Ranking high-quality paint systems using EIS. Part I: intact coatings, Corros. Sci. 45 (1) (2003) 123–138.
[60] Y. Zuo, R. Pang, W. Li, J. P. Xiong, Y. M. Tang, Y. M. . (2008). The evaluation of coating performance by the variations of phase angles in middle and high frequency domains of eis, Corros. Sci. 50(12) (2008) 3322-3328.
[61] S. Skale, V. Doleček, M. Slemnik, Substitution of the constant phase element by Warburg impedance for protective coatings, Corros. Sci. 49 (3) (2007) 1045–1055.
[62] T. Liu, Y. Liu, Y. Ye, J. Li, F. Yang, H. Zhao, L. Wang, Corrosion protective properties of epoxy coating containing tetraaniline modified nano-α-Fe_2O_3, Prog. Org. Coat. 132 (2019) 455–467.
[63] T. Ohtsuka, Raman spectra of passive films of iron in neutral borate solution, Mater Trans., JIM 37 (1996) 67–69.
[64] S.J. Oh, D. Cook, H. Townsend, Characterization of iron oxides commonly formed as corrosion products on steel, Hyperfine Interact. 112 (1998) 59–66.
[65] L. Wang, Y. Zhang, Y. Park, L. Chen, Y.M. Jung, Quantitative determination of iron ions based on a resonance raman (RR) probe-phenanthroline, Anal. Sci. 33 (1) (2017) 23–27.
[66] A. Schönemann, H.G.M. Edwards, Raman and ftir microspectroscopic study of the alteration of chinese tung oil and related drying oils during ageing, Anal. Bioanal. Chem. 400 (4) (2011) 1173–1180.
[67] S.M. Lashgari, H. Yari, M. Mahdavian, B. Ramezanzadeh, G. Bahlakeh, M. Ramezanzadeh, Application of nanoporous cobalt-based ZIF-67 metal-organic framework (MOF) for construction of an epoxy-composite coating with superior anti-corrosion properties, Corros. Sci. 178 (2021), 109099.
[68] S. Xiao, X. Cao, Z. Dong, X. Ma, X. Zhang, G. Cai, A pH-responsive cerium-imidazole decorated ZIF-8 to achieve self-healing barrier property for epoxy coating on Al alloy by controlled release, Prog. Org. Coat. 163 (2022), 106640.
[69] H. Wang, Q. Zhou, Evaluation and failure analysis of linseed oil encapsulated self-healing anticorrosive coating, Prog. Org. Coat. 118 (2018) 108–115.